Available online at www.sciencedirect.com
SCIENCE DIRECT®
Journal of Nuclear Materials 351 (2006) 174–186
journal of nuclear materials
www.elsevier.com/locate/jnucmat

Microstructural development in advanced ferritic–martensitic steel HCM12A

T.R. Allen [a,*], L. Tan [a], J. Gan [b], G. Gupta [c], G.S. Was [c], E.A. Kenik [d], S. Shutthanandan [e], S. Thevuthasan [e]

[a] *Nuclear Engineering Department, University of Wisconsin, 1500 Engineering Drive, Madison, WI 53706, USA*
[b] *Idaho National Laboratory, Idaho Falls, ID, USA*
[c] *University of Michigan, Ann Arbor, MI, USA*
[d] *Oak Ridge National Laboratory, Oak Ridge, TN, USA*
[e] *Pacific Northwest National Laboratory, Richland, WA, USA*

Abstract

HCM12A is an advanced nominal 12Cr ferritic–martensitic steel designed for higher temperature operation and is under consideration for application in core components in Generation IV nuclear energy systems. This work provides information on the hardening and microstructural changes in HCM12A after irradiation using 2.0 MeV protons at 400 °C to 10 dpa and at 500 °C to 3 dpa, and using 5 MeV Ni-ions at 500 °C to 50 dpa. Following irradiation, changes in hardness were measured using Vickers hardness indentation, changes in microstructure and phase stability were studied using transmission electron microscopy, and changes in microchemistry were measured using scanning Auger microscopy and analytical electron microscopy. The hardness at 400 °C increases by roughly 70% and saturates by roughly 5 dpa. The microstructural changes contributing to this hardness increase are mainly the formation of precipitate phases. Hardness increases are much smaller at 500 °C. Chromium is enriched at grain boundaries prior to irradiation, likely due to grain boundary carbides, and increases further during irradiation at least partially due to radiation-induced segregation.
Published by Elsevier B.V.

PACS: 61.82.Bg; 68.37.Lp; 61.72.Qq; 62.20.Qp

1. Introduction

Because of their improved swelling resistance at high dose, ferritic–martensitic steels are favored as cladding and duct material for fast reactor systems. The 12Cr alloy HT9 was the most advanced cladding and duct material used in FFTF and EBR-II [1], both sodium-cooled fast reactors. Many Generation IV reactor systems are conceptualized such that they would operate at higher temperature than was achieved in these prototype sodium-cooled systems. The sodium-cooled fast reactor (SFR), the lead-cooled fast reactor (LFR), and the supercritical

* Corresponding author. Tel.: +1 608 265 4083; fax: +1 608 263 7451.
E-mail address: allen@engr.wisc.edu (T.R. Allen).

0022-3115/$ - see front matter Published by Elsevier B.V.
doi:10.1016/j.jnucmat.2006.02.014

water-cooled reactor (SCWR) all include advanced ferritic–martensitic steels in the list of potential candidate materials [2]. HCM12A (Grade 122) was developed as a third-generation nominal 12 Cr steel with an upper temperature limit approximately 55 °C higher than HT9, which has a limit of 565 °C [3]. Because of the potential improvement in cycle efficiency allowed by operating at higher temperature, the possibility of replacing HT9 with HCM12A is of interest to Generation IV reactor designers.

Only one irradiation experiment on the third-generation ferritic–martensitic steels has been carried out [4]. HCM12A, along with NF616 and T91 (also known as modified 9Cr–1Mo) (both nominal 9Cr alloys as compared to the 12Cr HCM12A), were irradiated at 300 °C (the temperature of the specimens was said to vary from 265 to 312 °C) in the mixed neutron spectrum of the High Flux Reactor (HFR) in Petten, the Netherlands. The Charpy impact properties measured following these Petten irradiations are listed in Table 1.

The ductile-to-brittle transition temperature increased for all three alloys, with the shift being larger for the HCM12A and NF616 than for modified 9Cr–1Mo. Even the modified 9Cr–1Mo developed a larger shift than normally observed. Previous irradiations of modified 9Cr–1Mo at 300 °C indicated a shift of around 100 °C [5]. Tensile properties indicated that the NF616 showed the least hardening followed by modified 9Cr–1Mo, and the HCM12A hardened the most. The higher than expected DBTT shifts were postulated to come from two possible sources. First, the samples might have been irradiated at a nominal temperature lower than 300 °C. Second, the presence of boron in these alloys, along with the thermal spectrum flux in the Petten reactor may have generated significant helium that then affected impact properties.

Because little information exists on the radiation response of HCM12A, this work examined the hardness changes as well as the microstructural and microchemical changes of HCM12A irradiated with 2.0 MeV protons at 400 °C and 500 °C and the microstructural and microchemical changes of HCM12A irradiated with 5 MeV Ni-ions at 500 °C. These ion irradiations are not substitutes for neutron irradiation, but are a complementary tool for understanding the microstructural changes that will occur under irradiation. Because ion irradiation occurs at much higher displacement rates than experienced in a typical reactor environment, a shift in temperature is required to obtain microstructures similar to that expected in a neutron environment [6]. A detailed study on using ion irradiation to understand radiation response in austenitic stainless steels under light water reactor conditions has shown the utility of the ion irradiation technique [7]. Because HCM12A could be used across a wide range of temperatures in Gen IV systems, these experiments provide a first look at possible microstructural changes.

2. Experiment

HCM12A was obtained in plate form from Sumitomo Metal Industries, Kashima Steel Works. The composition of HCM12A, as reported in the manufacturer's check chemistry, is listed in Table 2. Because of the low chromium concentration reported in the manufacturer's check chemistry, a second independent analysis was performed and indicated the chromium concentration was 11.3 at.%. The plate was normalized at 1050 °C followed by air-cooling and then tempered at 770 °C followed by air-cooling. Following the temper, the average grain size of the prior austenite grains is 14.3 ± 3.3 μm.

Proton irradiation was performed on 2 mm thick bars at the Michigan Ion Beam Laboratory using 2.0 MeV protons at a temperature of 400 °C to doses of 3, 7, and 10 dpa and at a temperature of 500 °C to a dose of 3 dpa [8]. Ni-ion irradiations were conducted at the Environmental and Molecular Science Laboratory at Pacific Northwest

Table 1
Charpy impact properties of steels irradiated in HFR [4]

Steel	Unirradiated		Irradiated		Property change	
	DBTT (°C)	USE (J)	DBTT (°C)	USE (J)	ΔDBTT (°C)	USE (J)
Mod. 9Cr–1Mo	−78	8.9	97	6.6	175	2.2
NF616	−41	7.3	209	4.5	249	2.8
HCM12A	−36	8.3	189	4.3	225	4.0

Miniature Charpy specimens were used. Irradiation was nominally to 2.5 dpa at 300 °C.

Table 2
Composition of HCM12A (wt%)-balance Fe

C	Si	Mn	P	S	Cu	Ni	W	Cr	Mo	V	Nb	Al	N	B
0.11	0.28	0.62	0.015	0.002	0.98	0.39	1.82	10.54	0.32	0.19	0.054	0.001	0.063	32[a]

[a] ppm.

National Laboratory using 5 MeV Ni-ions at 500 °C to doses of 5 and 50 dpa [9].

Microhardness was measured both prior to and after irradiation by protons. Vickers hardness was measured using a Vickers Microhardness Tester (Micromet-II). Indents at a load of 25 g were applied on a 2 mm bar in both the irradiated region and the unirradiated region. Since proton irradiation produces a fairly uniform damage layer over only the first 17 μm, a low load of 25 g with load time of 20 s was applied to ensure that the unirradiated material below the damaged layer was not being sampled. The center-to-center spacing of indents was approximately 100 μm, so that specimen deformation from one indent does not affect results of neighboring indentations. Approximately 25 indents were taken for each irradiation condition.

TEM discs were punched from the irradiated materials using a disc punch to a diameter of 2.3 mm. The discs were then mechanically wet polished from the unirradiated side down to roughly 70 μm thickness to minimize the magnetic interference with the electron beam in the microscope. For samples irradiated with 5 MeV Ni-ions, a maximum ion penetration depth of approximately 1.5 μm into ferritic–martensitic steels occurs. A thin layer of approximately 0.5 μm depth was removed from the irradiated side using a 5-s jet electro-polishing with a solution of 2% perchloric acid and 15% ethylene glycol in methanol at a polishing condition of 25 V and −65 °C. TEM discs were then jet-polished from the unirradiated side to perforation.

For samples irradiated with protons, samples were back-thinned and then electropolished to create thin area in the first 15 μm from the irradiated surface. For 2 MeV protons, the penetration depth is approximately 20 μm with a flat damage profile up to 17 μm in depth. The 2.3 mm disc sample was mounted to a 50 μm thick and 3-mm diameter Cu slot grid using epoxy to provide a 3 mm diameter TEM disc.

Microstructure characterization was carried out using a JEOL 2010 200 kV transmission electron microscope equipped with EDS for chemical analysis. Microstructural characterization has been performed for the 500 °C Ni-ion irradiated samples and the 400 °C proton-irradiated samples. Analysis of the 500 °C proton irradiated samples will be reported in future work.

A PHI 670 scanning Auger electron microprobe was used to analyze microchemistry at interfaces in the proton irradiated samples. To promote intergranular fracture, samples were cathodically charged with hydrogen in a solution of 0.1 N sulphuric acid with the addition of As_2O_3 as a poison for recombination of hydrogen. Samples were fractured in situ at a pressure of 1×10^{-9} Torr by bending with a special fracture stage attached to the Auger vacuum chamber. Once the fracture was achieved, a secondary electron image of the fracture surface was obtained to identify the areas of the sample that failed intergranularly. Analyses in an area of about 1 μm^2 were performed on grain boundary facets, channeled fracture areas, and on ductile fractures for comparison. Auger spectra from 30 to 1000 eV were recorded from every point analyzed at a beam energy of 10 keV. Semiquantitative calculations of chemical composition are reported as atomic concentration calculated following Davis et al. [10]. Sensitivity factors of iron, chromium, copper, and nickel have been obtained by comparing calculated concentration at the ductile areas of as-received sample to the composition of the material.

Prior austenite grain boundary compositions were measured using scanning transmission electron microscopy with energy dispersive X-ray spectrometry (STEM/EDS). The STEM/EDS was performed at an accelerating voltage of 200 kV on a Philips CM200 equipped with a field emission gun source at the Oak Ridge National Laboratory. STEM/EDS measurements were performed at the grain boundary and at increments of 1.0 nm away from the boundary to give compositional profiles. The incident probe thickness was approximately 1.4 nm (full width, tenth maximum). The sample was tilted towards the X-ray detector and each grain boundary analyzed was aligned such that the boundary was 'edge-on' (parallel to the electron beam). This alignment minimizes the effect of geometric

broadening of the measured profiles by an inclined boundary. To find prior austenite grain boundaries, samples were examined a low magnification in a Phillips XL30 FEG/SEM. The prior austenite grain boundaries are decorated with precipitates. A map is made of the boundaries intersecting the edge of the thin foil which assisted in locating the boundaries in the CM200.

3. Results

Microhardness was used to estimate changes in mechanical properties during irradiation. Hardness measurements were performed on samples irradiated with protons to varying doses. The change in hardness results for HCM12A are presented in Fig. 1 along with those T91 [11,12] for comparison. For both HCM12A and T91 irradiated at 400 °C, the hardness increases at low dose and appears to saturate near 5 dpa. At 500 °C, both HCM12A and T91 show a slight, but similar increase in hardness by 3 dpa. The T91 irradiated at 450 °C (which is a separate lot from the T91 irradiated at 400 °C and 500 °C) shows a hardening trend that falls between the 400 °C and 500 °C data for T91 and HCM12A.

The microstructure of unirradiated HCM12A mainly consists of precipitates that are distributed both at grain boundaries and in the matrix. The diffraction pattern and EDS analysis of the precipitates

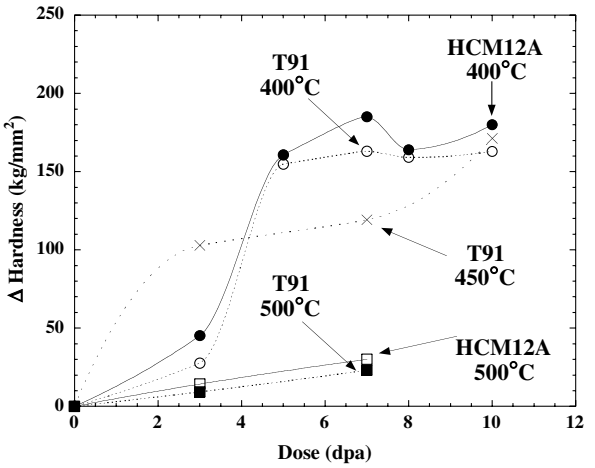

Fig. 1. Change in hardness as a function of radiation dose. Uncertainty in the measurements is smaller than the data points used in the figure. Each point averages approximately 25 separate indents.

revealed nearly all the precipitates in the unirradiated case are $M_{23}C_6$ with a FCC lattice parameter of 1.06 nm and a typical composition of approximately (in wt%) 65%Cr, 30%Fe, 3%W, 1.5%Mo in addition to carbon (carbon was not measured). Dislocation density varied dramatically, ranging from dislocation free to the dense areas with tangled and complex dislocation configuration. No dislocation loops are seen in the unirradiated material. The general views of the unirradiated microstructure and the detailed arrangement of dislocations are shown in Figs. 2(a) and 3(a).

For the sample irradiated with Ni-ions to 5 dpa, there is no significant change in microstructure, as shown in Figs. 2(b) and 3(b). No cavities were found. No dislocation loops were identified. The precipitates examined were still dominated by $M_{23}C_6$, but a few vanadium–niobium precipitates were identified from EDS analysis, with a typical composition of approximately 50%V, 17%Cr, 17%, 12%Nb. Fig. 4 shows various precipitates suspended on a film formed during jet-polishing, giving an opportunity for a better measurement of precipitate composition than is possible with EDS of precipitates embedded in the matrix. Among the precipitates in the picture, those marked p04, p08, and p11 are V–Nb precipitates and the rest are mostly $M_{23}C_6$ precipitates. Fig. 4 also shows the EDS spectrum of $M_{23}C_6$ and V–Nb precipitates. The overall dislocation density appeared slightly increased as shown in Figs. 2 and 3. No quantitative measurement on dislocation density was attempted due to its non-uniform distribution and extremely high density in some areas.

The microstructure of HCM12A irradiated to 50 dpa is similar to that at 5 dpa as demonstrated in Figs. 2(c) and 3(c). Again, no voids were found at higher dose. However, some dislocation loops were found in areas with a dense dislocation population. No significant changes in dislocation configuration occurred although the overall dislocation density appeared to further increase compared to the 5 dpa case. The microstructure at 50 dpa is still dominated by a dense dislocation network and $M_{23}C_6$ precipitates.

For alloy HCM12A irradiated with 2.0 MeV protons at 400 °C to 10 dpa, dislocation loops, micro voids, and finely distributed small precipitates were observed in addition to the dislocations and $M_{23}C_6$ presented in the unirradiated condition. Fig. 5 contrasts the general microstructure at low magnification between the unirradiated and the 10 dpa samples. At this low magnification, there is very little

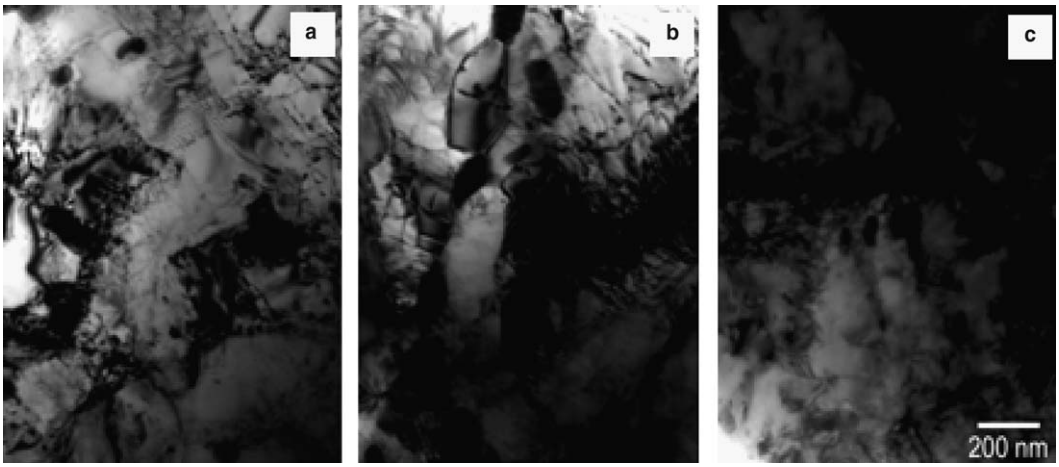

Fig. 2. Low magnification TEM micrographs showing the microstructure of alloy HCM12A (a) in the unirradiated condition and irradiated at 500 °C to (b) 5 dpa and (c) 50 dpa.

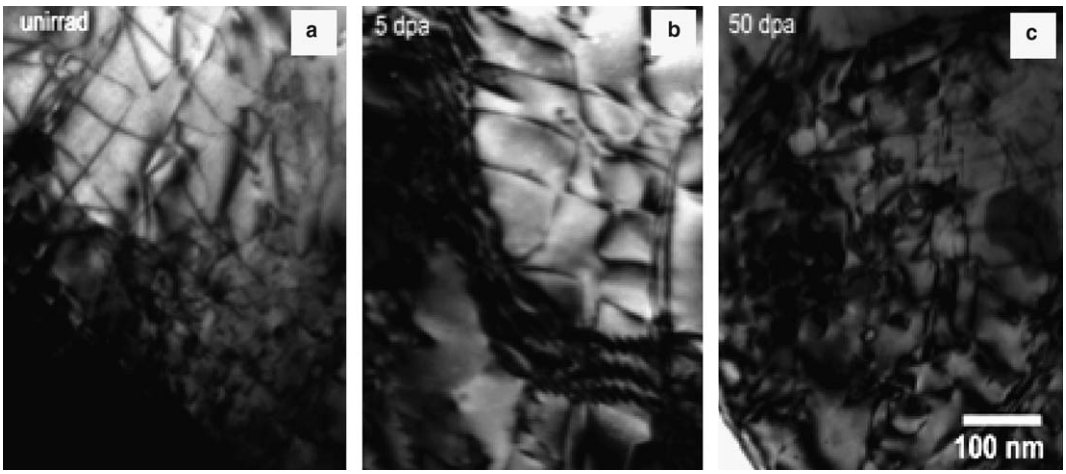

Fig. 3. Low magnification TEM micrographs showing the microstructure of alloy HCM12A (a) in the unirradiated condition and irradiated at 500 °C to (b) 5 dpa and (c) 50 dpa.

noticeable difference in Fig. 5 except the presence of small spots in the irradiated sample. The loops shown in Fig. 6 are identified as $a_0[1\,0\,0]$ type (a_0 is lattice constant), with an average size of 34 nm and density of $3.2 \times 10^{20}\ m^{-3}$. Micro-voids and radiation-induced small precipitates imaged from the same area are shown in Fig. 7. The average size and volume for voids is 6.2 nm and 154 nm^3, respectively. The void density is $9.4 \times 10^{14}\ cm^{-3}$ and the calculated void swelling is 0.015%. The small precipitates have an average size of 5.7 nm with a density of $3.9 \times 10^{15}\ cm^{-3}$. Assuming the precipitate composition can be roughly represented by a composition of 50%V, 17%Cr, 17%, 12%Nb, the measured size and density of these small precipitates does not account for all the V and Nb in the HCM12A alloy. The V and Nb not in these small precipitates may be in large precipitates not included in this analysis, be in precipitates too small to image, be in solid solution, or may be accounted for by varying composition of precipitates. The 3D stereo images of these small precipitates revealed that these small precipitates are not surface features and they are distributed uniformly in the matrix. The composition and crystal structure of these small precipitates could not be determined due to their small sizes compared to the size of the EDS excited volume.

Grain boundary composition was measured using Auger electron spectroscopy. For the AES analysis, intergranular fracture was obtained under

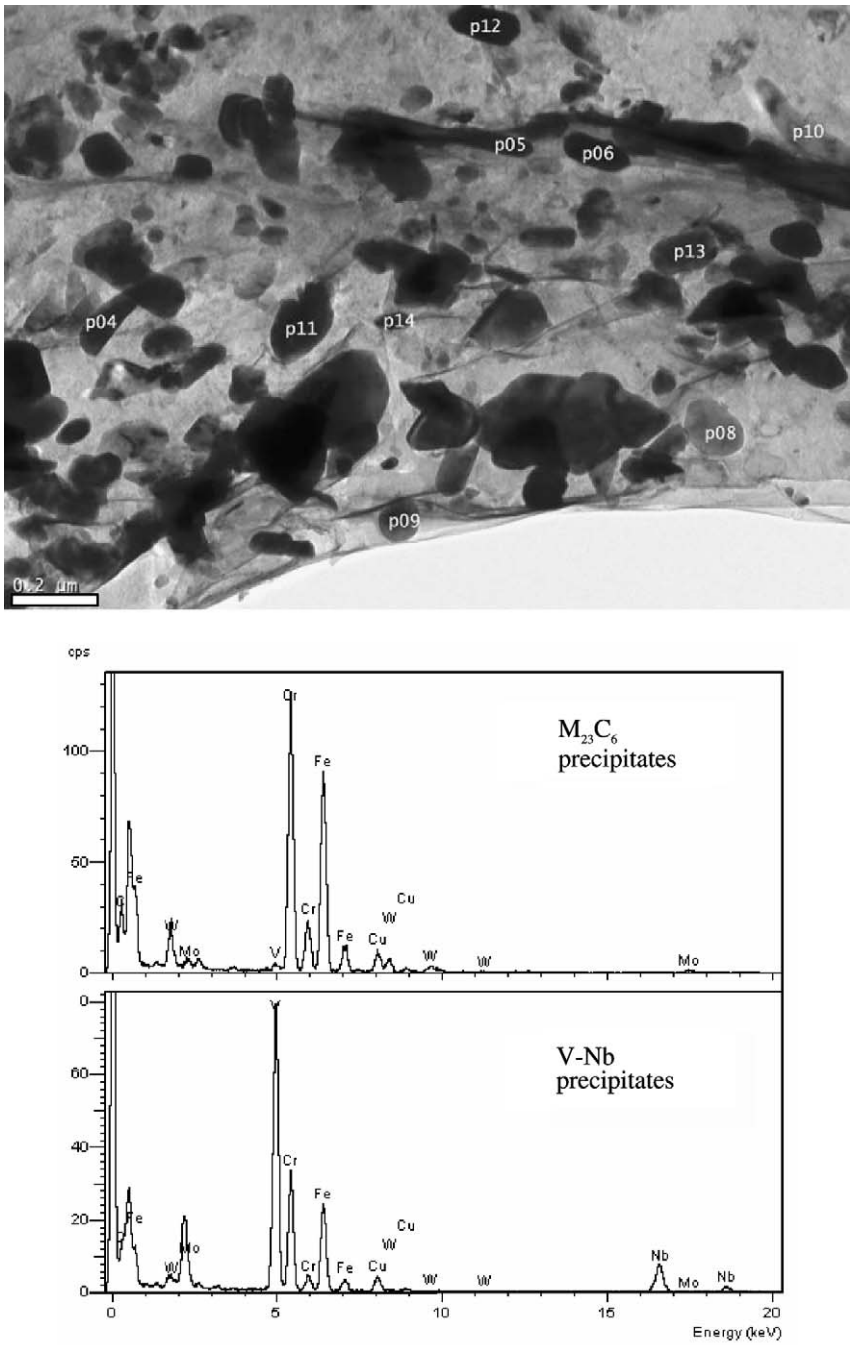

Fig. 4. Precipitates in HCM12A irradiated with Ni-ions at 500 °C to 5 dpa. Those marked p04, p08, and p11 are V–Nb precipitates. The rest are mostly $M_{23}C_6$ type precipitates.

all conditions although the percentage area that fractured intergranularly was low. The percentage of intergranular features exposed in the proton-irradiated samples is lower for the unirradiated (normalized and tempered) material. Fig. 8 shows, as an example, secondary electron images of a fracture surface obtained from the unirradiated material. In general, the fracture surfaces showed ductile areas (Fig. 8(b)) in the inner part of the sample away from the fracture initiation side, and intergranular areas (Fig. 8(c)) close to the fracture initiation side. Closer to the fracture initiation side of the sample, areas of

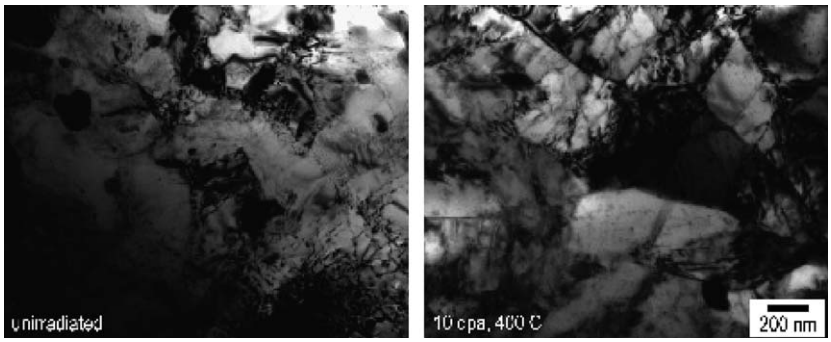

Fig. 5. Overview of the HCM12A microstructure for the unirradiated (left) and the proton irradiated at 400 °C to 10 dpa. General features remains similar for both cases. Burgers vector analysis for loops was carried out using $\mathbf{g}\cdot\mathbf{b}$ analysis. Images were taken using $g = 011$ and $g = 200$ near zone $\langle 011\rangle$ for this analysis.

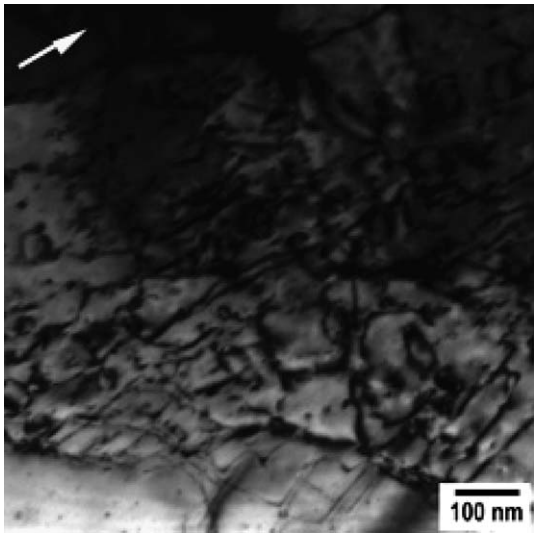

Fig. 6. Dislocation loops in HCM12A irradiated with protons at 400 °C to 10 dpa. The image was taken using $g = 110$ (shown by the arrow) near zone [122]. The loops are identified as a_0[100] loops.

cleavage (or possibly partial intergranular fracture) were also exposed during fracture of the proton irradiated samples.

Fig. 9 shows, as an example, Auger spectra of a proton irradiated sample obtained from a ductile area and from an intergranular facet. The intergranular facets are likely to correspond to prior austenite grain boundaries. The AES technique alone cannot differentiate between composition change due to radiation-induced segregation or changes in precipitate concentration. In ductile areas, the main alloying elements, iron and chromium, and also copper, nickel, and oxygen were identified. Spectra from areas of intergranular fracture show the same elements as the ductile areas plus the presence of silicon and phosphorus. The phosphorous was not detectable at all intergranular facets. In addition to the spectra from ductile and intergranular areas, spectra were analyzed from areas of cleavage as shown in Fig. 9(c). One of the images of the cleavage area is shown as an inset of Fig. 9(c). Compared to intergranular areas, a higher oxygen signal was measured in the ductile and cleavage areas. The higher oxygen concentration may be caused by the larger surface area at the rough ductile area that promotes the adsorption of oxygen more readily than the smooth intergranular facets.

Semi-quantitative analysis for the elements Cr, Fe, Ni, Cu, and P are listed in Table 3. Oxygen and carbon were not included in the analysis because they are subject to errors due to environmental contamination during long-time examination. The Ni concentration is likely overestimated although the Auger peak range of Ni1 for quantitative analysis was selected carefully to minimize the influence of the partial overlap of the Auger peak of Cu2 on Ni1. Since phosphorous segregation is not typically noted on cleavage fracture surfaces, the areas identified as cleavage in this report may contain partial IG fracture. The reported P average concentration for intergranular facets does include facets with no measurable concentration in the calculation.

The segregation of Cr, Fe, Ni, and Cu at intergranular and cleavage areas are compared to the ductile area is shown in Fig. 10. The data from the 3 dpa irradiation at 500 °C, as well as the data from 3, 7, and 10 dpa irradiations at 400 °C are included in Fig. 10. The segregation of Cr and Fe increases with irradiation dose and temperature.

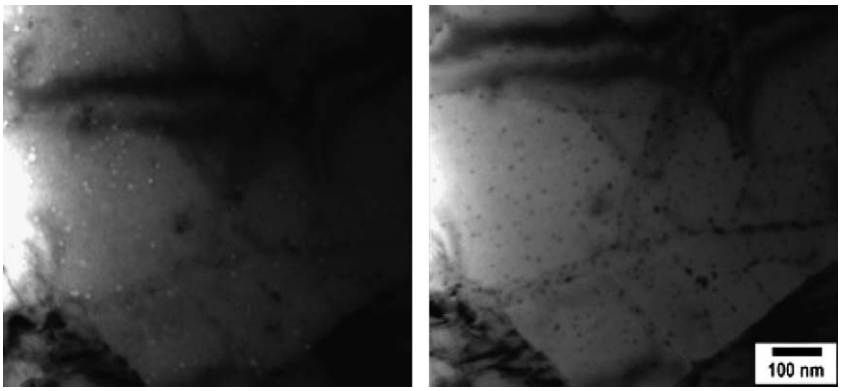

Fig. 7. Micro-voids and radiation-induced small precipitates imaged from the same area in HCM12A irradiated with protons at 400 °C to 10 dpa. The image on the left is taken in an under-focused condition showing voids and the image on the right is an in-focus image showing small precipitates.

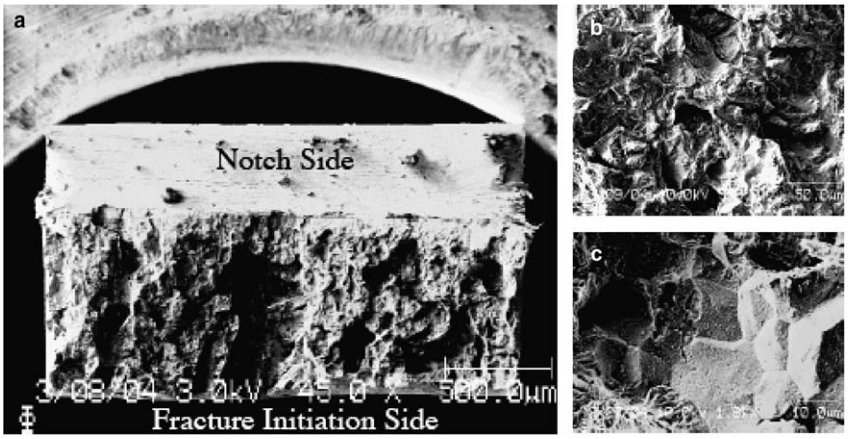

Fig. 8. SEM images of (a) overview, (b) ductile area and (c) intergranular area of the fracture surface of an as-received sample obtained in the Auger vacuum chamber.

The irradiation effect on the segregation of Cu and Ni follows a complex trend. Cu and Ni have the same segregation trends at intergranular areas during radiation. Different irradiation-induced segregation trends of Cu and Ni are observed at cleavage areas indicating a different segregation mechanism than that seen on the intergranular facets or that the cleaved areas represent varying mixtures of ductile and intergranular fracture.

To a limited extent in this work, grain boundary segregation was measured using STEM-EDS. The dual challenges of finding a precipitate-free area on a prior austenite grain boundary plus the difficulty of working with highly magnetic samples limited the segregation data that was collected. A single precipitate-free area (precipitates are located greater than 500 nm from the portion of the boundary profiled) on a prior austenite grain boundary was analyzed on a sample irradiated at 500 °C to 5 dpa with Ni-ions. The composition of the nearest precipitates, as well as the Cr profile across the boundary, is shown in Fig. 11. A slight enrichment of Cr, as compared to the bulk concentration, was measured. Although not shown on the figure, Fe was depleted and silicon enriched at the boundary. Chromium enrichment and iron depletion in T91 irradiated with protons at 450 °C was also recently measured [11]. The predominance of measurements indicate Cr enrichment and Fe depletion in irradiated 9–12 Cr FM steels.

4. Discussion

4.1. Hardness

Busby et al. have recently developed a correlation between yield strength and hardness for austenitic

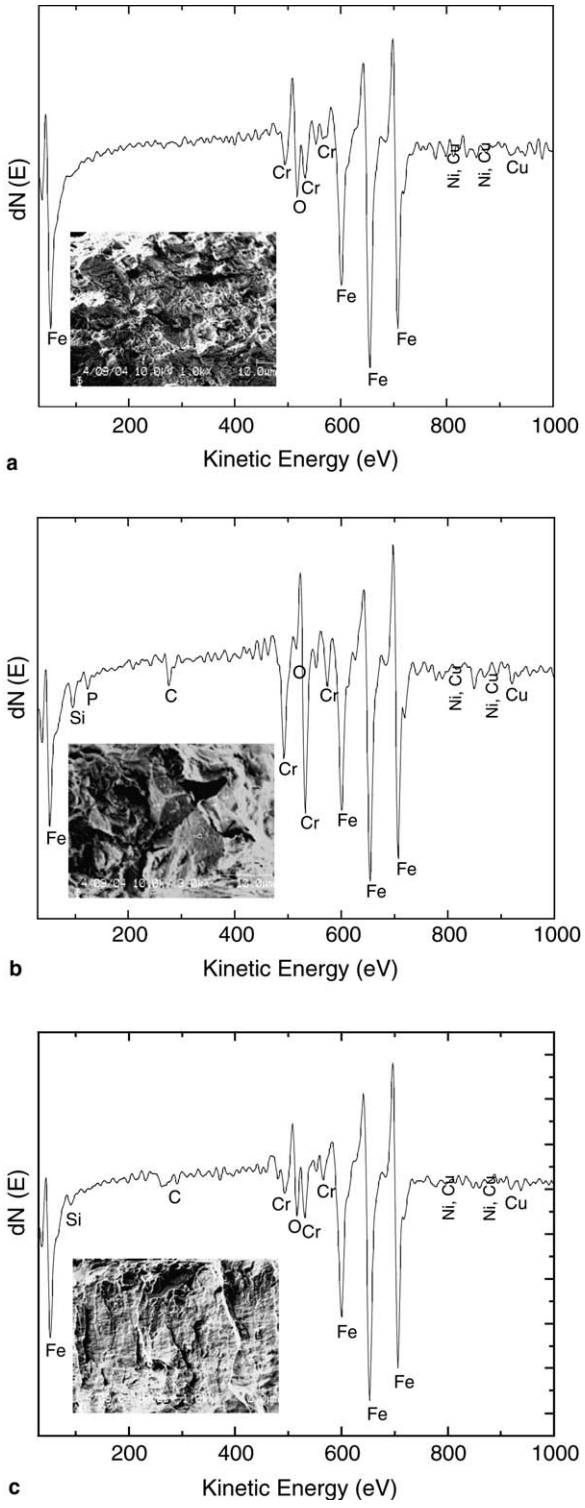

Fig. 9. Auger spectra obtained from a sample irradiated with protons at 400 °C to a dose of 7 dpa: (a) ductile area, (b) intergranular facet, and (c) cleavage area.

and ferritic (pressure vessel) steels [13]. The relation for pressure vessel steels is shown in Eq. (1). The correlation factor for austenitic steels was 3.03. Because the correlation was similar between austenitic and ferritic steels, this work will assume the factor of 3.06 is a reasonable estimate for converting hardness to yield strength for the 12Cr steel HCM12A. Using factor of 3.06, the calculated change in yield strength due to radiation at 400 °C to 10 dpa is 550 MPa. At 500 °C to 3 dpa, the change in hardness is much smaller and the estimated increase in yield strength is roughly 30 MPa,

$$\Delta\sigma_y(\mathrm{MPa}) = 3.06\Delta H_v\left(\frac{\mathrm{kg}}{\mathrm{mm}^2}\right). \quad (1)$$

The increase in hardness is similar for the both HCM12A and T91, indicating the irradiation-induced increase in yield strength is similar. Although there was some concern that the copper additions to HCM12A may lead to larger hardening than in earlier generations of 9–12 Cr ferritic–martensitic steels, these limited hardness results do not indicate that this will be a problem.

For comparison, the hardness increase of T91 irradiated with protons at 450 °C to 10 dpa is also plotted in Fig. 1. The hardness increase of T91as a function of dose at 450 °C falls between the HCM12A hardness increases at 400 °C and 500 °C. Since the hardening of these steels is a strong function of temperature, the trends seen in Fig. 1 appear reasonable.

Klueh and Alexander performed tensile tests on 9Cr–1MoVNb (corresponding to T91) and 12Cr–1MoVW (corresponding to HT9) in both HFIR (doses of 8–11 dpa and 37–72 dpa) and EBR-II (doses of ~16 dpa) [5]. The HFIR experiments showed that the yield strength increases occurred early in the radiation with only small changes occurring between 8–11 and 37–72 dpa. Yield strength changes were larger for the higher Cr concentration alloy and larger in the thermal spectrum reactor HFIR. As changes in hardness and yield strength are proportional for metals, the hardness data of this work is consistent with the work of Klueh with hardening increasing with bulk chromium concentration.

4.2. Microstructure

There were no voids, no radiation-induced precipitates, and only few scattered loops identified in Ni-ion irradiated HCM12A while all of these features were found in the proton-irradiated samples.

Table 3
Average atomic concentration calculated from Auger spectra of the specimen irradiated with a dose of 3 dpa at 500 °C, and 3, 7, 10 dpa at 400 °C

			Cr	Fe	Ni	Cu	P
As-received		D	11.7 ± 0.7	85.7 ± 0.8	0.5 ± 0.1	0.9 ± 0.1	0.03
		IG	17.6 ± 2.1	79.2 ± 2.2	0.6 ± 0.2	1.1 ± 0.2	0.04
3 dpa	400 °C	D	11.9 ± 0.9	85.2 ± 1.8	0.6 ± 0.1	1.0 ± 0.2	0.03
		C	12.2 ± 0.9	83.3 ± 1.0	0.8 ± 0.1	1.2 ± 0.2	0.06
		IG	19.1 ± 1.6	75.6 ± 2.3	0.9 ± 0.3	2.0 ± 0.3	0.07
	500 °C	D	11.9 ± 1.0	86.4 ± 2.2	0.4 ± 0.1	0.9 ± 0.3	0.03
		C	14.6 ± 1.5	80.9 ± 2.5	0.5 ± 0.1	1.3 ± 0.1	0.11
		IG	21.5 ± 1.2	71.7 ± 1.8	0.5 ± 0.1	1.4 ± 0.2	0.16
7 dpa (400 °C)		D	11.8 ± 1.4	85.3 ± 1.5	0.6 ± 0.1	1.0 ± 0.2	0.03
		C	13.4 ± 1.5	82.8 ± 2.2	0.7 ± 0.3	1.2 ± 0.3	0.08
		IG	24.8 ± 2.4	69.9 ± 2.0	0.8 ± 0.2	1.9 ± 0.4	0.11
10 dpa (400 °C)		D	11.9 ± 0.9	85.3 ± 0.9	0.5 ± 0.1	1.0 ± 0.2	0.03
		C	16.2 ± 2.1	79.8 ± 2.5	0.5 ± 0.2	1.3 ± 0.3	0.10
		IG	25.9 ± 2.6	69.5 ± 2.6	0.4 ± 0.2	1.5 ± 0.3	0.14

Note: Characters D, C, and IG denote ductile, cleavage, and intergranular areas, respectively. Uncertainty is the standard deviation of the measurements.

Proton irradiation at lower temperature and lower dose produced more visible radiation damage than Ni ion irradiation at higher temperature and higher dose. Mansur has derived expressions that can be used to estimate the temperature shift required to obtain similar microstructures when the dose rate of the irradiation varies [14]. To obtain similar loss rates of point defects to sinks for a 7.0×10^{-6} dpa/s (protons) and 1.4×10^{-3} dpa/s (Ni-ions) requires a temperature shift of approximately 50 °C. Because the proton irradiation was carried out at 100 °C lower temperature than the Ni-ion irradiation, the difference in radiation damage microstructures is likely to be partially due to temperature. As noted in the discussion on hardness, the hardness (and therefore yield strength and associated microstructure) changes rapidly as a function of temperature from 400 °C to 500 °C.

The increase in precipitate density (assumed to be V–Cr–Nb based on the Ni-ion irradiations but detailed examination of extraction replicas from materials irradiated at 400 °C is required to make a definitive statement) plus the increase in dislocation loops is likely to be responsible for the radiation hardening in alloy HCM12A at 400 °C. Very limited dislocation loops and voids were noted in the 50 dpa Ni-ion irradiated sample, so irradiation damage features typically associated with hardening have not developed by 50 dpa at 500 °C in HCM12A. The microstructural development of the Ni-ion irradiated HCM12A was very similar to that of T91 irradiated at 500 °C to 50 dpa [15]. This lack of microstructural features is not in agreement with the work of Schaeublin et al. [16] who did observe loops in ferritic–martensitic alloys at 1–2 dpa. The hardness increases at low dose may also be related to some precipitation, such as alpha prime phase, which is extremely difficult to observe in TEM, or invisible nanodefects and/or nanovoids that contribute to the hardening. The alpha prime phase is known to be more likely to form as the bulk chromium concentration in the alloy increases.

4.3. Segregation

For austenitic stainless steels, chromium is depleted at the grain boundary during radiation. As discussed above, the TEM analysis showed Cr-rich grain boundary carbides in the unirradiated HCM12A. Chromium concentration was observed to further increase with irradiation in this study. The enrichment of chromium could be related to the formation of new chromium-rich precipitates, e.g., carbides and phosphides [17–21], or the growth of existing carbides, possibly enhanced by radiation. This is consistent with the review of Maziasz [21] that indicated that the irradiation-induced phases in martensitic/ferritic steels are all Cr-rich, in contrast to the Cr-poor phases induced in the austenitic steels. Even though such precipitation could result in Cr-depletion at the grain boundaries between the precipitates, FEG/STEM measurements indicate an increase in grain boundary chromium concentration associated with radiation-induced segregation.

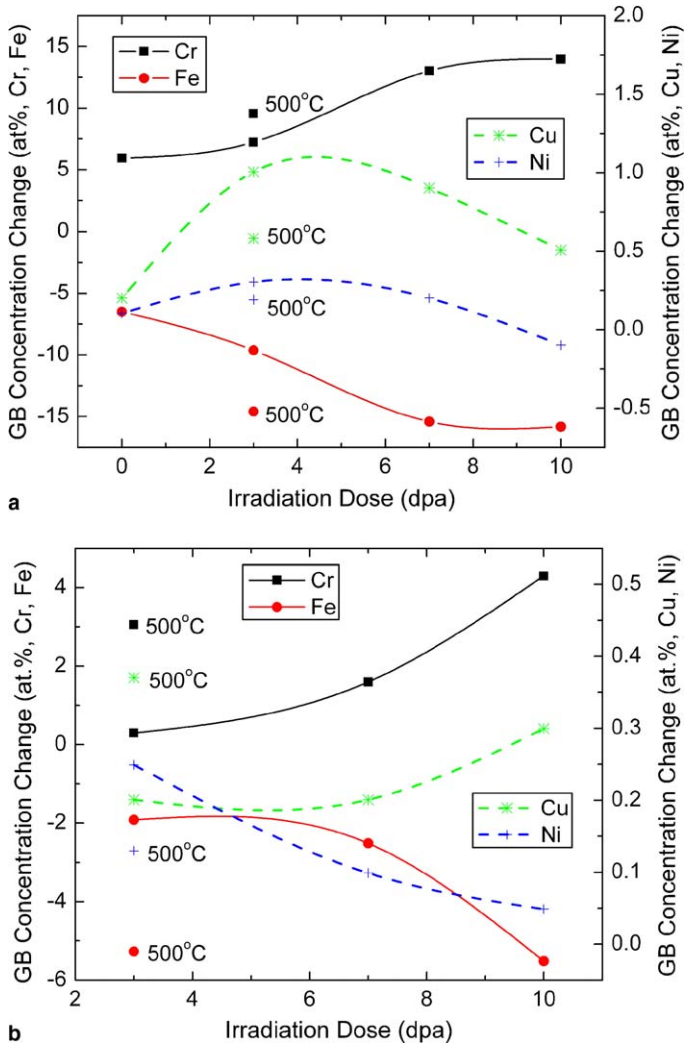

Fig. 10. Irradiation effect on the grain boundary concentration of Fe and Cr as major elements and of Cu and Ni as minor elements at (a) intergranular and (b) cleavage areas. The data from the irradiation at 500 °C to 3 dpa is included, in addition to the data from the irradiation at 400 °C.

Segregation has previously been measured in irradiated ferritic–martensitic steels. Takahashi, using 650 keV electron irradiation at 400 °C on Fe–5Cr and Fe–13Cr binary alloys [22] and Mahon et al. irradiating Fe–11.8Cr–0.58Mn using both 1 MeV electrons and 52 MeV Cr ions at 550 °C [23] found Cr depletion and Fe enrichment at boundaries. Morgan irradiated FV448 using fast neutrons at 465 °C to 46 dpa and found Fe depletion and Cr enrichment at lath boundaries [20]. Clausing et al. irradiated HT9 using fast neutrons at 410 °C to 13 dpa and also found Fe depletion and Cr enrichment at lath boundaries [17]. Low angle lath boundaries are not expected to have significant segregation, so the measurements in Clausing's work might be related to precipitate formation. Ohnuki et al. [24] irradiated Fe–Cr model alloys with 200 keV C and found Cr enrichment at grain boundaries. For the work of both Takahashi and Mahon, the measured profiles were large (>100 nm) compared to typical radiation-induced segregation profiles. The profiles measured by Morgan and Clausing are much narrower and typical of RIS. Although neither Takahashi nor Mahon reported precipitates affecting their grain boundary segregation measurements, the width of the profiles indicates something other than RIS was occurring. Many cases of very broad profiles have been reported when irradiating thin foil

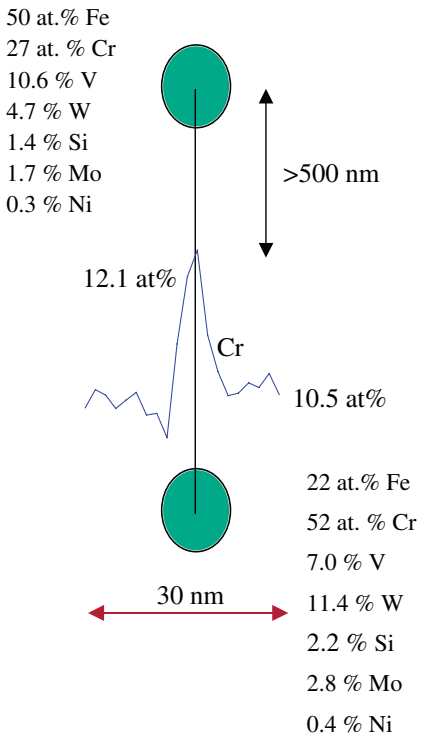

Fig. 11. Schematic of grain boundary segregation as measured in HCM12A irradiated with 5 MeV Ni-ions at 500 °C to 5 dpa.

samples with high-energy electrons. Brimhall et al., [25] used 5 MeV Ni-ions to radiate HT9 at 500–600 °C to doses of 0.8 dpa and found P enrichment at the surface, similar to the trends in this study.

Models have been developed for predicting RIS in austenitic stainless steels. The most advanced models (known as modified inverse Kirkendall (MIK) models) take into account local composition when calculating diffusional energies [26]. Although these models have not been optimized for BCC steels, a model calculation using a base composition of Fe–10.5Cr–0.4Ni (corresponding to HCM12A) does predict Cr enrichment during radiation, consistent with the limited STEM-EDS data from this study. Extrapolation of diffusion coefficients measured in an Fe–13Cr alloy by Kucera [27] indicate Cr is a faster diffuser than Fe in the ferromagnetic state but slower in the paramagnetic state. The segregation may depend on specific alloy processing.

The enriched chromium at the grain boundaries (and associated depletion off-boundary) has potential implication for Generation IV lead-cooled fast reactors as well as supercritical water-cooled reactors. Sensitization issues experienced in light water reactors due to carbide precipitation might also be possibilities in supercritical water or in lead-alloy coolants as grain boundary composition changes could lead to corrosion or stress corrosion cracking susceptibility, or liquid metal embrittlement.

4.4. Future studies

This work has presented an early look at microstructural changes of HCM12A under radiation. HCM12A is also being irradiated in the ATR reactor to obtain low dose thermal spectrum response. Plans exist to irradiate HCM12A in the PHENIX reactor to get high dose, fast spectrum response. Concurrent testing of the corrosion response of HCM12A in both supercritical water and lead-alloys is also underway.

5. Conclusions

The ferritic–martensitic steel HCM12A was irradiated with 2.0 MeV protons at 400 °C to a dose of 10 dpa, at 500 °C to a dose of 3 dpa, and with 5 MeV nickel ions at 500 °C to 50 dpa. The hardness of HCM12A at 400 °C increases with dose, saturating after approximately 5 dpa with an approximate 70% increase in hardness. Using hardness-yield strength correlations, this corresponds to a 520–550 MPa yield strength increase. The increase in hardness appears to be attributable to precipitate formation and slight increases in dislocation loop density. Hardness increases are much smaller after irradiation at 500 °C.

Chromium is enriched and iron is depleted at boundaries containing precipitates in the unirradiated state. The higher chromium concentration at the boundaries in the unirradiated state is likely due to chromium carbides. Irradiation causes further increases in chromium concentration and decreases in iron concentration at the boundaries. This could be due to coarsening of existing carbide particles, nucleation of new carbide particles, or radiation-induced segregation of chromium to the boundary away from carbides. Initial FEG/STEM studies indicate that chromium enrichment due to RIS is at least partially contributing to the increase in grain boundary chromium concentration. Since grain boundary chromium carbide precipitation could cause chromium depletion on the boundary between precipitates, the measured enrichment may be less than would be seen on a precipitate free boundary.

Acknowledgements

This material is based upon work supported by the US Department of Energy under the NERI program Award No. DE-FG07-03ID14542 and NERI Project Number 02-110. Thanks to the staffs of the Michigan Ion Beam Laboratory, the Michigan Electron Microscopy Analysis Laboratory, and the Wisconsin Material Science Center.

References

[1] R.D. Leggett, L.C. Walters, J. Nucl. Mater. 204 (1993) 23.
[2] T.R. Allen, D.C. Crawford, in: Proceedings of ICAPP '03, American Nuclear Society, Cordoba, Spain, 2003, paper 3237.
[3] R. Viswanathan, W.T. Bakker, in: Proceedings of the 2000 International Joint Power Generation Conference, Miami Beach, FL, July 2000, p. 1.
[4] M. Horsten, M.G.E. van Osch, D.S. Gelles, M.L. Hamilton, in: M.L. Hamilton, A.S. Kumar, S.T. Rosinski, M.L. Grossbeck (Eds.), Effects of Irradiation on Materials: 19th International Symposium, ASTM STP 1366, American Society for Testing and Materials, West Conshohocken, PA, 2000, p. 579.
[5] R.L. Klueh, D.J. Alexander, J. Nucl. Mater. 187 (1992) 60.
[6] L.K. Mansur, J. Nucl. Mater. 216 (1994) 97.
[7] G.S. Was, T.R. Allen, J.T. Busby, J. Gan, D. Damcott, D. Carter, M. Atzmon, E.A. Kenik, J. Nucl. Mater. 270 (1999) 96.
[8] D.L. Damcott, J.M. Cookson, R.D. Carter, J.R. Martin, M. Atzmon, G.S. Was, Nucl. Instrum. Meth. Phys. Res. B99 (1995) 780.
[9] S.M. Bruemmer, M.D. Merz, L.A. Charlot, J. Nucl. Mater. 186 (1991) 13.
[10] L.E. Davis, N.C. MacDonald, P.W. Palmberg, G.E. Riach, R.E. Weber, Handbook of Auger Electron Spectroscopy, Physical Electronics Industries, Eden Prairie, MN, 1976.
[11] N. Ham, this proceedings.
[12] G.S. Was, J.T. Busby, T.R. Allen, J. Gan, Sixth International Meeting on Nuclear Applications of Accelerator Technology (AccApp '03), American Nuclear Society, LaGrange Park, IL, June 2003, p. 864.
[13] J.T. Busby, M.C. Hash, G.S. Was, J. Nucl. Mater. 336 (2005) 267.
[14] L.K. Mansur, J. Nucl. Mater. 216 (1994) 97.
[15] J. Gan, T.R. Allen, J.I. Cole, S. Ukai, S. Shutthanandan, S. Thevuthasan, Materials Research Society Proceedings, vol. 792, Materials Research Society, 2004, p. 13.
[16] R. Schaeublin, D. Gelles, M. Victoria, J. Nucl. Mater. 307&311 (2002) 197.
[17] R.E. Clausing, L. Heatherly, R.G. Faulkner, A.F. Rowcliffe, K. Farrell, J. Nucl. Mater. 141&143 (1986) 978.
[18] T. Kato, H. Takahashi, S. Ohnuki, K. Nakata, J. Kuniya, J. Nucl. Mater. 179&181 (1991) 623.
[19] H. Takahashi, T. Kato, S. Watanabe, N. Sakaguchi, Ann. Phys. 20 (C3) (1995) 109.
[20] T.S. Morgan, E.A. Little, R.G. Faulkner, J. Titchmarsh, in: R.E. Stoller, A.S. Kumar, D. Gelles (Eds.), Effects of Radiation in Materials 15th International Symposium, ASTM STP 1125, American Society for Testing and Materials, Philadelphia, 1992, p. 633.
[21] P.J. Maziasz, J. Nucl. Mater. 169 (1989) 95.
[22] H. Takahashi, S. Ohnuki, T. Takeyama, J. Nucl. Mater. 103&104 (1981) 1415.
[23] G.J. Mahon, A.W. Nichols, I.P. Jones, C.A. English, T.M. Williams, in: D.I.R. Norris (Ed.), Proceedings Symposium on Radiation-induced Sensitisation of Stainless Steels, CEBG, Berkeley Nuclear Laboratories, 1987, p. 99.
[24] S. Ohnuki, H. Takahashi, T. Takeyama, J. Nucl. Mater. 104 (1982) 1121.
[25] J.L. Brimhall, D.R. Baer, R.H. Jones, J. Nucl. Mater. 122&123 (1984) 196.
[26] T.R. Allen, G.S. Was, Acta Metall. 46 (1998) 3679.
[27] J. Kucera, K. Stransky, Mater. Sci. Eng. 52 (1981) 1.